This article was published in Acta Materialia 169 (2019) 15-27, https://doi.org/10.1016/j.actamat.2019.02.029 and Acta Materialia 199 (2020) 425-428, https://doi.org/10.1016/j.actamat.2020.08.050

Engineering Strain and Conductivity of MoO_3 by Ion Implantation

Daniela R. Pereira[1,2,3,4*], Carlos Díaz-Guerra[5], Marco Peres[1], Sérgio Magalhães[1], João G. Correia[3], José G. Marques[3], Ana G. Silva[6], Eduardo Alves[1], Katharina Lorenz[1,2*]

1) IPFN, Instituto Superior Técnico, Universidade de Lisboa, Estrada Nacional 10, km 139.7, 2695-066 Bobadela LRS, Portugal

2) Instituto de Engenharia de Sistemas de Computadores-Microsystems and Nanotechnology (INESC-MN), Lisboa, Portugal

3) C2TN, Instituto Superior Técnico (IST), Campus Tecnológico e Nuclear, Estrada Nacional 10, km 139.7, 2695-066 Bobadela LRS, Portugal

4) Departamento de Física, Faculdade de Ciências e Tecnologia, Universidade Nova de Lisboa, Portugal

5) Departamento de Física de Materiales, Facultad de Ciencias Físicas, Universidad Complutense de Madrid, Madrid, Spain.

6) Cefitec, Departamento de Física, Faculdade de Ciências e Tecnologia, Universidade Nova de Lisboa, Campus da Caparica, 2829-516, Caparica, Portugal

E-mail: danielapereira@ctn.tecnico.ulisboa.pt, lorenz@ctn.tecnico.ulisboa.p

Abstract

α-MoO_3 lamellar crystals are implanted with 170 keV oxygen ions at room temperature and with fluences between 1×10^{12} cm^{-2} and 1×10^{17} cm^{-2}, in order to modify the electrical and structural properties of the crystals. A controllable and significant increase of the electrical conductivity, over several orders of magnitude, is observed after implantation at high fluences. Based on high resolution X-ray diffraction (HRXRD) and micro-Raman spectroscopy measurements, this effect is attributed to the formation of donor-type defect complexes and new phases more conductive than the α-MoO_3 orthorhombic phase. A significant expansion of the *b* lattice parameter, increasing with fluence, is observed as a response to the defects created by implantation. Strain build-up occurs in several steps and in distinct depth regions within the implanted layer. Contrary to the typical values reported for other implanted oxide materials, an unusually high maximum perpendicular deformation of ~3% is verified.

Keywords: Molybdenum oxide, Implantation/irradiation, X-ray diffraction (XRD), Raman spectroscopy, Electrical properties

1. Introduction

Molybdenum oxide (MoO_3) is a n-type semiconductor with a band gap between 2.8 and 3.2 eV, which has demonstrated a high potential for several applications [1] such as biosensors [2], gas sensors [3], solar cells [4] and lithium ion batteries [5]. MoO_3 may exhibit different crystal phases, such as orthorhombic α-MoO_3, monoclinic β-MoO_3 and hexagonal *h*-MoO_3. However, only the α-MoO_3 phase is thermodynamically stable at room temperature [6]. The α-MoO_3 phase is constituted by an orthorhombic unit cell with the lattice parameters a = 3.9624Å, b = 13.860Å and c = 3.6971Å [7], having a lamellar structure in the [010] direction. Each layer consists of double layers of distorted MoO_6 octahedra, with various distances between molybdenum and oxygen atoms ranging from 1.67 to 2.33 Å [8], as shown in Figure 1.

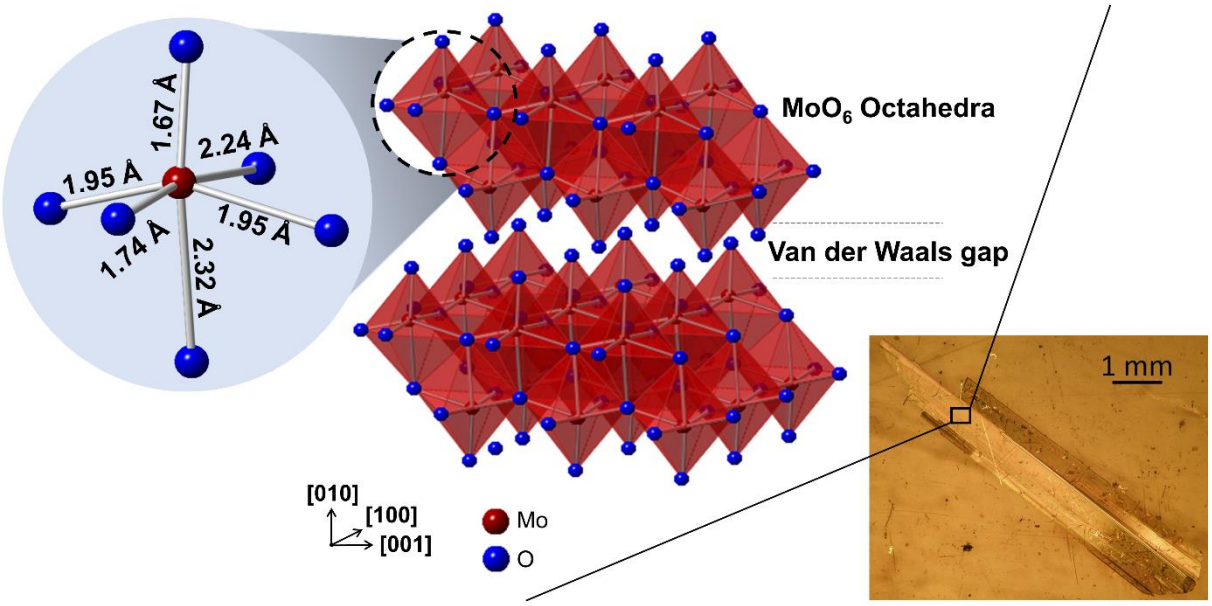

Figure 1 – Optical microscopy image of an as-grown, lamellar MoO_3 sample (right); the crystalline structure of orthorhombic α-MoO_3 (middle); the distances between oxygen and molybdenum atoms that constitute a MoO_6 octahedra (left).

The nature of the bonds between the octahedra of the same or adjacent layers is also different, i.e., in the direction [010] the bonds are of the Van der Waals type and in the directions [100] and [001] the bonds are of the covalent type [8]. The resulting Van der Waals gap of this 2-dimensional structure (see Figure 1) is an important feature for many of the applications named above, since it allows the easy intercalation of atoms or accommodation of defects. The concentration of defects, namely the presence of oxygen vacancies, plays a dominant role in determining the electrical properties of MoO_3, due to the increase of the free electron concentration, associated with a decrease of the band gap [9,10]. Thus, by controlling the concentration of these defects, it is possible to modify the insulating behavior of stoichiometric MoO_3 and to achieve a semiconductor or even semi-metallic behavior. This is, indeed, observed in the MoO_{3-x} ($2<x\leq3$) and MoO_2 phases, respectively [8,11]. Alteration of the stoichiometry of MoO_3 can be performed during the

growth process, adjusting the growth conditions, or by annealing processes in atmospheres with low oxygen partial pressure [11,12]. The intercalation of foreign elements in the MoO_3 lamellar structure, as well as the creation of oxygen vacancies can also give rise to intermediate states within the band gap. For example, intercalated H^+ ions may interact with the oxygen atoms forming hydrogen bronze structures (H_xMoO_3), which can dissociate in MoO_{3-x} and water [13,14]. On the other hand, doping can also be used to control the physical properties of the material and increase its potential for various applications. As reported by H.-Y. Chen *et al.*[4], it is possible to increase the hole concentration and electrical conductivity of amorphous nanowires and films of MoO_3 by indium doping. Contrary to what happens in the intrinsic MoO_3 that has a high mobility of holes but high electrical resistivity, indium doped MoO_3 exhibits high optical transparency and low electrical resistivity, which demonstrates the potential of this material as a p-type transparent conductive oxide to be used in transparent electronic applications. Doping by ion implantation was used to incorporate optically active rare earth elements [15]. Kr implantation was shown to significantly increase the electrical conductivity of MoO_3 samples [16]. For the high fluences studied in this publication, the changes in electrical properties were attributed to amorphization and subsequent recrystallization in the MoO_2 phase [16]. In addition, it has also been shown recently that the conductivity of MoO_3 can be increased over several orders of magnitude by electron irradiation [17]. Furthermore, the controlled induced lattice strain along a single axis can allow tuning of the electrical, optical and magnetic properties of oxides, as observed in films of WO_3 [18] and $La_{0.7}Sr_{0.3}MnO_3$ [19] when implanted with low-energy helium ions.

In this work we report the modification of the electrical and structural properties of α-MoO_3 lamellar crystals by ion implantation, which were evaluated by high resolution X-ray diffraction (HRXRD) micro-Raman spectroscopy and I-V curves. These measurements show that, at high fluences, the conductivity can be increased by several orders of magnitude using ion implantation, which is a technique routinely applied in semiconductor industry. This conductivity gain is stable over time in comparison to what is observed when oxygen vacancies are created by annealing. Concerning structural properties, an increase of the *b* lattice parameter in several steps with increasing fluence is verified reaching an unusually high maximum deformation of ~3%.

2. Experimental Details

MoO_3 lamellar crystals were grown by an evaporation-solidification method described in detail in references [15,20]. A disc of compacted Mo powder with 7 mm diameter and 2 mm thickness was placed at the center of a horizontal tube furnace, at a temperature of 750 ºC during 10 h in an air flow of 2 l/min using compressed air. The heating of the disc promotes the oxidation of the Mo by direct contact with air. MoO_3 will then deposit at the cooler ends of the tube where the temperature is about 400-450 ºC. This method allows to obtain MoO_3 lamellar crystals (an image of a typical sample is shown in figure

1) with typical thicknesses between 100 nm and 10 μm and lateral dimensions of about 2×5 mm^2. However, approximately 70% of them have thicknesses in the (2-4) μm range [15]. XRD measurements show a preferred crystallographic orientation with the surface normal along the [010] direction. This orientation is a consequence of the layered structure present in the orthorhombic α-MoO_3 phase, as a result of the lower growth rate in this direction, which is in agreement with previous studies of single crystals and nanoflakes of MoO_3 [21,22].

For the implantation, MoO_3 lamellar crystals were mounted on Si or on glass substrates. Ion implantation was performed at room temperature and along the direction normal to the surface, using oxygen ions with an energy of 170 keV and fluences in the range from 1×10^{12} cm^{-2} to 1×10^{17} cm^{-2}. Note that ion channeling effects are minimized due to the lamellar structure of the crystal and relative tilt of the crystallites. The maximum ion flux used was about 1.6×10^{13} ions. cm^{-2}. s^{-1} for the fluence of 1×10^{17} cm^{-2}. As-implanted samples were characterized at the structural level by XRD in a Bruker D8 Discover high resolution diffractometer using a Göbel mirror, a 0.2 mm collimation slit and a 2-bounce Ge (220) monochromator to select the Cu K_{α_1} radiation in the primary beam. In the secondary beam, a 0.1 mm slit was placed in front of a scintillation detector. It is worth to mention that, despite the inhomogeneous nature of the crystal (see Fig. 1), where different crystallites are tilted relative to each other, in the 2θ-θ configuration the alignment is done for crystallites with the same orientation. Although irregularities in the lamellar structure may affect the quality of XRD patterns (peak widths and fringe patterns), typical full width of half maximum (FWHM) values of ~0.04º of the measured (060) 2θ–θ scans revealed a good crystalline quality of the starting material.

The diffractograms were fitted using the RaDMax software [23], which allowed us to obtain the strain and static Debye-Waller (DW) factor profiles and, consequently, to discuss the mechanisms of defect formation with depth resolution. The static DW factor is used to take into account the lattice damage and has values that range from 1 (for a perfect crystal) to 0 (for a fully damaged crystal) [24]. For these fits, the software uses the classical Levenberg-Marquardt least-squares algorithm. Following SRIM simulations [25], a fixed implanted layer thickness of 500 nm was considered.

Micro-Raman measurements were carried out at room temperature in a Horiba Jobin-Yvon LabRAM HR800 system with an UV excitation source (325 nm He-Cd laser), on an Olympus BX 41 confocal microscope with a 40x objective. A charge coupled device (CCD) detector was used to collect the scattered light dispersed by a 1200 lines mm^{-1} grating. The spectral resolution of this system is 1.5 cm^{-1} and the diameter of the laser spot on the samples is ~ 2 μm. Using the Beer-Lambert law, the UV laser beam penetration depth was estimated to be in a range of 37 to 60 nm, which is well below the implanted layer thickness obtained by the SRIM simulations (~500 nm). Thus, the observed changes in the Raman spectra after the ion implantation are due to the implanted layer only and do not have any contribution from the non-implanted material.

Finally, electrical characterization was performed on selected samples using an Agilent B1500A Device Analyzer to perform I-V curves. In this equipment, the maximum measurable resistance is in the order of hundreds of megaohms. Two co-planar indium contacts were deposited, by placing two stripes of In on top of the sample with a distance of about 2 mm between them and then heating the sample to ~150 ºC. Once the In stripes have melted, the sample was cooled to ambient temperature and the contacts solidified. For the realization of the electrical measurements when using Si substrates, Kapton tape was used as insulating layer between the MoO_3 flake and the substrate. For glass substrates the crystals were directly attached by the In-contacts. By comparing the results obtained in these different devices, no differences were observed proving the similarity of the configurations.

3. Experimental Results

3.1. High resolution X-ray diffraction measurements

Figure 2 shows HRXRD 2θ-θ scans around the 060 reflection for as-grown and as-implanted samples. The main Bragg peak (at 2θ=38.95º marked by the vertical dashed line) is observed in all diffractograms and corresponds to the deep, unimplanted region of MoO_3. For samples implanted with the lowest fluence of 1×10^{12} cm^{-2} (not shown), no change was observed after implantation. For higher fluences, an additional peak or a shoulder at 2θ values lower than that of the main Bragg peak is observed, which reveals an expansion of the *b* lattice parameter in the implanted region. This satellite peak is observed at 2θ=38.90º for 5×10^{12} cm^{-2} and then shifts towards lower angles with increasing fluence to 2θ=38.52° for 7.5×10^{13} cm^{-2}. The high definition of this peak for these low fluences suggests that the perpendicular strain induced by implantation defects is quasi-homogeneous along the implanted layer. At 1×10^{14} cm^{-2}, the satellite peak becomes less well-defined, suffering broadening and splitting in multiple peaks, indicating that there was a loss of homogeneity. Nevertheless, the maximum strain value continues to increase with increasing fluence. When the fluence increases to 5×10^{14} cm^{-2} and 1×10^{15} cm^{-2}, the maximum strain does not appear to change significantly with respect to the fluence of 1×10^{14} cm^{-2}. However, the diffraction intensity drops, which reveals a worse crystalline quality. Surprisingly, with a further increase of the fluence to values above 1×10^{15} cm^{-2}, the maximum strain appears to increase again. The low scattered intensity seen for the fluences 5×10^{14} cm^{-2} and 1×10^{15} cm^{-2} suggests that the layer suffering direct impact by the implanted ions is strongly damaged. Consequently, the higher scattered intensity at low 2θ angles and the existence of multiple peaks for fluences of 5×10^{15} cm^{-2} and 1×10^{16} cm^{-2}, suggest that the changes observed in the experimental diffraction patterns originate predominantly from different depths compared to previous fluences. For fluences of 5×10^{16} cm^{-2} and 1×10^{17} cm^{-2} no further evolution of the diffraction patterns is observed. The low scattered intensity from the damaged regions of

these samples, suggests that most of the region affected by the implantation was highly damaged, or possibly amorphized.

The perpendicular deformation values corresponding to each 2θ value are included in Figure 2, obtained by the expression $\varepsilon_{\perp} = (b_{impl} - b_0)/b_0$, where b_0 denotes the b lattice parameter of the as-grown sample and b_{impl} is the b lattice parameter value that corresponds to each 2θ value of the obtained diffractogram.

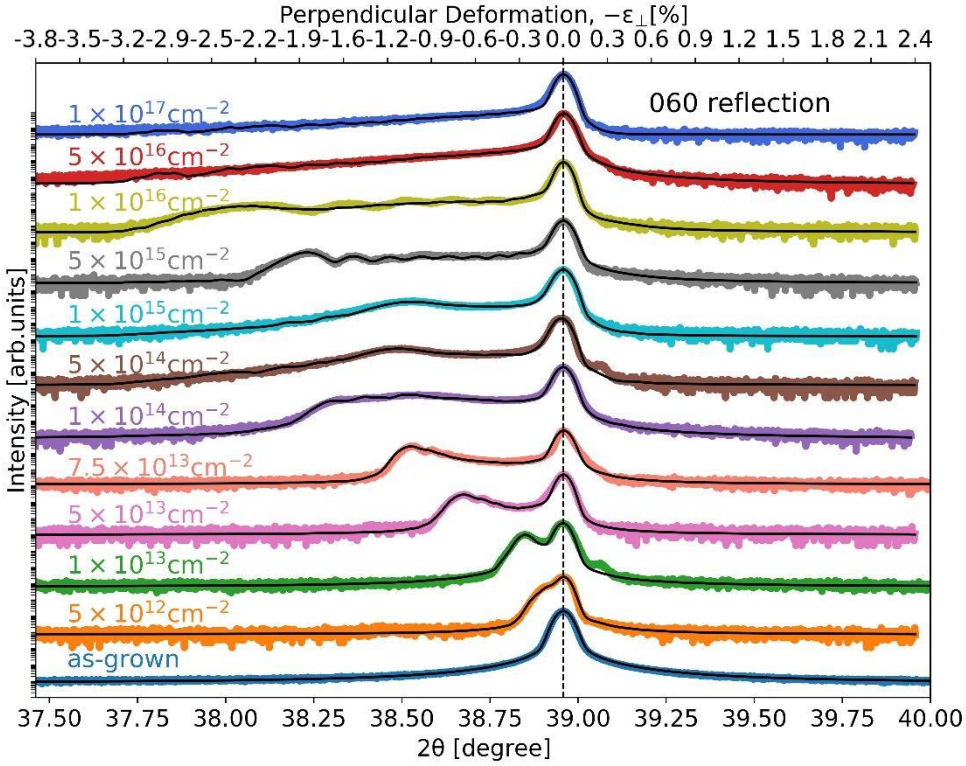

Figure 2 – HRXRD 2θ-θ scans around the 060 reflection performed in an as-grown sample and as-implanted samples of MoO_3 implanted with fluences ranging from 5×10^{12} cm^{-2} to 1×10^{17} cm^{-2} (colored symbols) and respective simulated curves (black lines) using the RaDMaX software. The perpendicular deformation, $-\epsilon_{\perp}$, is also shown at the top of the graph. In some diffractograms, the presence of a peak at angles higher than the main Bragg peak is due to the K_{α_2} line of the Cu resulting from an incomplete filtration by the monochromator. The main Bragg peak is marked by the dashed line.

In order to get more information about the profile and evolution of the strain along the implanted depth, the XRD diffractograms obtained were fitted using the software RaDMaX (radiation damage in materials analyzed with X-ray diffraction) [23]. The fits are included in Figure 2 (black lines) and show very good agreement with the experimental curves for all samples. The extracted strain and damage profiles – the latter described by the static DW factor – are presented in Figure 3.(a) and Figure 3.(b), respectively. Figure 3.(c) shows the concentration profiles of implanted ions and oxygen vacancies obtained by SRIM 2013 (Stopping and Ranges of Ions in Matter) Monte Carlo simulations [25], for an implantation of oxygen ions with an energy of 170 keV and

considering the fluence of 5×10^{12} cm^{-2} (displacement energies of 25 eV and 28 eV were used for Mo and O, respectively, which correspond to the values suggested by SRIM).

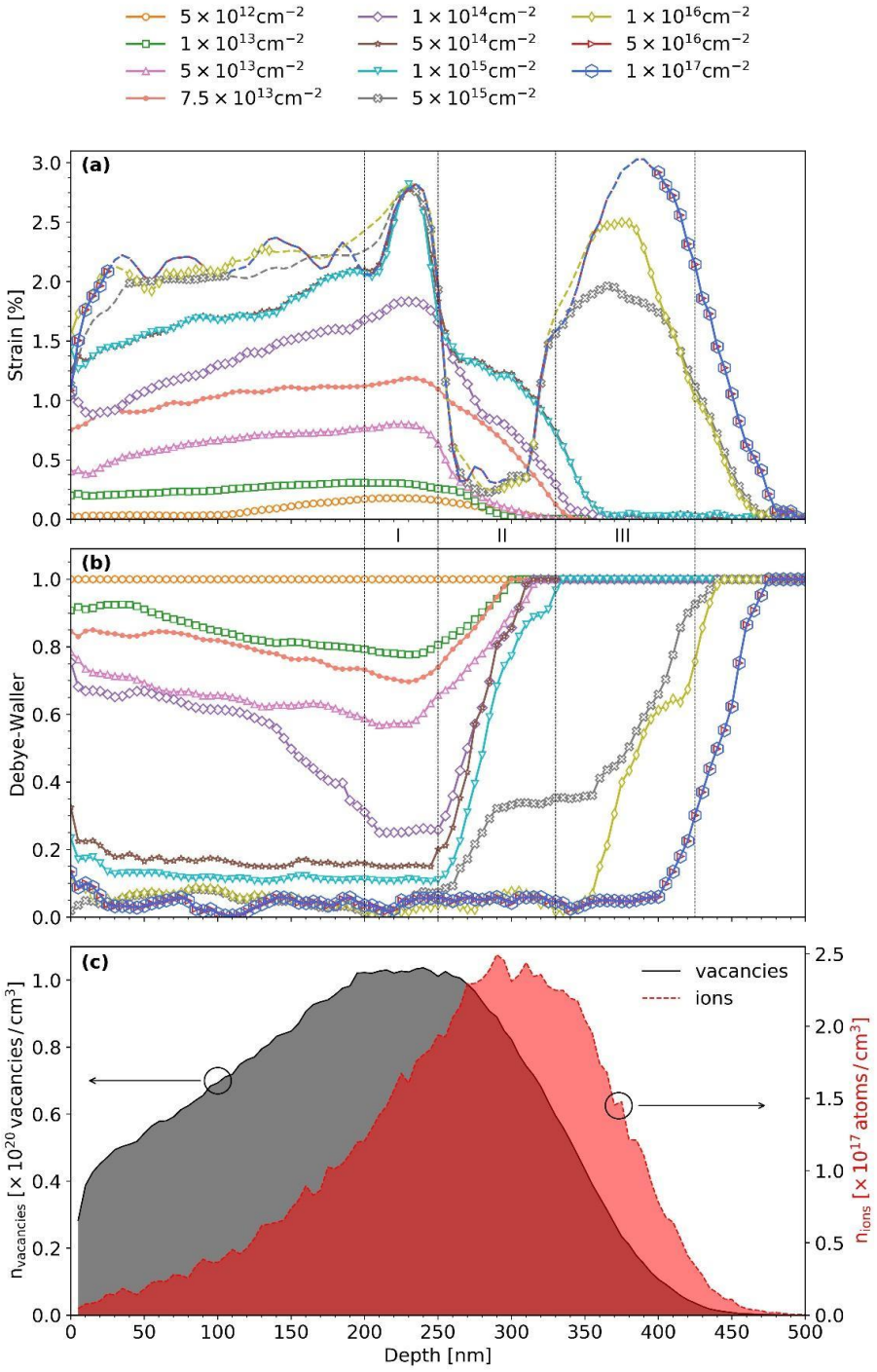

Figure 3 – (a) Strain profiles and (b) static DW factor profiles obtained by simulation of the XRD diffractograms presented in Fig.2, using the RaDMaX software; (c) Concentration profiles of oxygen vacancies and implanted oxygen ions obtained from SRIM simulations for a fluence of 5×10^{12} cm^{-2}. Different depth regions are marked for which the average strain and static DW factor are plotted in Fig.5.

For fluences below 1×10^{14} cm^{-2}, excellent fits are achieved assuming strain and defect profiles, which agree well with the expected defect distribution calculated by SRIM. A gradual increase of the maximum strain and damage, accompanied by a slight widening of the strain/damage profiles is observed with increasing fluences. The perpendicular strain is almost constant in a wide region of the implanted layer, which leads to the well-defined peaks observed in the diffractograms shown in Figure 2. Starting at 1×10^{14} cm^{-2}, the profiles indicate that the perpendicular strain distribution becomes more inhomogeneous, which may result from the migration of defects as well as from the formation of point defect clusters and extended defects. In fact, comparing the strain profile for this fluence with the SRIM simulations (Figure 3.(c)), it is possible to conclude that the maximum strain still occurs in a region where the concentration of the formed oxygen vacancies is maximum (region I in Figure 3), i.e., in a region with a high concentration of primary defects due to nuclear interaction. On the other hand, the strain profile now extends to deeper regions of the sample close to the end of range of the implanted oxygen ions (region II in Figure 3). Although no chemical effects are expected for oxygen implantation (such as the formation of new chemical compounds), the change in stoichiometry may alter the defect dynamics or favor the formation of O_2. The increasingly inhomogeneous profiles are in accordance with the diffractograms presented in Figure 2, where the well-defined satellite peaks typical for low fluences are no longer observed for fluences above 7.5×10^{13} cm^{-2}. For the fluences of 5×10^{14} cm^{-2} and 1×10^{15} cm^{-2}, no significant change of the strain profiles is observed. Furthermore, the static DW factor is very low for depths smaller than 250 nm, which means that this implanted region is highly damaged, not having a significant contribution to the obtained diffractograms. Thus, the XRD signal is dominated, essentially, by region II where the static DW factor is much larger. Results for these intermediate fluences indicate a radical change in structural and elastic properties leading to a strain saturation for these fluences. This behavior probably results from an alteration of defect morphology (e.g. the formation of dislocation loops and stacking faults), which can lead to a relaxation of the strain as well as to a loss of elasticity of the lattice. Similar effects have been observed in other compound semiconductors such as in GaN and $Al_xGa_{1-x}N$ as well as oxides (for example ZnO), and were attributed to the re-arrangement of initial defect clusters into extended defects such as dislocation loops or stacking faults [26–30].

When the fluence increases to values above 1×10^{15} cm^{-2}, a strong increase of strain with fluence is observed at a depth between 330 and 425 nm (region III in Figure 3). According to the SRIM simulations (Figure 3.(c)), this new peak appears in a region where the nuclear interactions and thus primary defect formation are very low. This increase of strain in region III may result from a migration of point defects from the region of higher nuclear interaction to deeper regions in the sample. On the other hand, it is important to note that, for fluences above 1×10^{15} cm^{-2}, in several depth regions the DW factor drops to very low values leading to ill-defined strain values. Therefore, when the DW factor drops below 0.06, the strain values are shown as dashed lines in figure 3.(a) indicating that the

crystals are so damaged that the diffracted intensity coming from these regions is negligible and, consequently, the perpendicular deformation values cannot be estimated.

Selecting the maximum value in the entire strain profile for all fluences – Figure 3.(a) – the evolution of the maximum strain as a function of the fluence is shown in Figure 4. Thus, for fluences below 5×10^{13} cm^{-2}, the maximum strain increases slowly with the fluence, followed by a significant increase at fluences between 5×10^{13} cm^{-2} and 5×10^{14} cm^{-2} and, subsequent saturation up to 1×10^{16} cm^{-2}. Above 1×10^{16} cm^{-2}, a new increase of the maximum strain occurs, leading to a second plateau starting at 5×10^{16} cm^{-2}. The strain values in this plateau correspond to the maximum trustable strain value achieved. An increase of damage, in several steps, as a function of the implantation fluence is very common in materials where point defects are mobile during implantation, since this mobility allows the recombination and interaction of defects. Thus, similar damage build-up curves were for example reported for Rutherford backscattering spectrometry/channeling (RBS/C) measurements in GaN and ZnO [29], III-V arsenides and phosphides [31] and also for less direct techniques such as optical reflectance in Si [32], where damage accumulation proceeds in different steps until eventually amorphization is induced. Concerning strain build-up, the present behavior is rather unusual since, typically, strain builds up with increasing fluence until reaching a critical value. In this threshold value, the crystal order breaks down either by amorphization or by severe alterations of the microstructure leading to saturation or even relaxation of the strain. Such behavior was observed in a wide range of materials including various oxides [27,30,33–35]. Interestingly, in most of these reports, the maximum perpendicular strain supported by the crystal structure is below the values found in MoO_3 (up to 3% – Figure 3.(a)).

As mentioned above, the damage build-up in multiples steps is a typical behavior of many semiconductors and has been successfully described by the model introduced by N. Hecking *et al.*[32] where the formation of point defects, point defect clusters and the creation of the amorphous regions are considered. Recently, an adaptation of this model was presented by G.Velişa *et al.* [36] considering the formation of defect clusters by direct impact and by stimulated growth, separately. Thus, the total damage is composed of the sum of the fractions of point defects (f_{pd}), defect clusters (f_{c/c_1}) and amorphous regions (f_{a/c_2}), which are described by the following three differential equations:

$$df_{pd}/dN_i = \sigma_{pd}\left(1 - f_{a/c_2} - f_{c/c_1} - f_{pd}\right) - \sigma_r f_{pd} - \left[\left(\sigma_{c/c_1} + \sigma_{cs/cs_1} f_{c/c_1}\right) + \left(\sigma_{a/c_2} + \sigma_{as/cs_2} f_{a/c_2}\right)\right] f_{pd} \quad (1)$$

$$df_{c/c_1}/dN_i = \left(\sigma_{c/c_1} + \sigma_{cs/cs_1} f_{c/c_1}\right)\{1 - (f_{c/c_1} + f_{pd})/[f_s\left(1 - f_{a/c_2}\right)]\} - (\sigma_{a/c_2} + \sigma_{as/cs_2} f_{a/c_2}) f_{c/c_1} \quad (2)$$

$$df_{a/c_2}/dN_i = (\sigma_{a/c_2} + \sigma_{as/cs_2} f_{a/c_2})(1 - f_{a/c_2}) \quad (3)$$

In which $f_{pd} = [\sigma_{pd}/(\sigma_{pd} + \sigma_r)]\{1 - \exp\left[-\left(\sigma_{pd} + \sigma_r\right)N_i\right]\}$ (4)

and, $f_{a/c_2} = 1 - (\sigma_{a/c_2} + \sigma_{as/cs_2})/\{\sigma_{as/cs_2} + \sigma_{a/c_2} \exp[(\sigma_{a/c_2} + \sigma_{as/cs2})N_i]\}$ (5)

The formation of point defects is predominant for low fluences, and the concentration of these defects is influenced by their formation (σ_{pd}) and recombination (σ_r) cross-sections. Defect clusters can be formed within a single ion impact (σ_{c/c_1}) or by stimulated growth of the clusters already existing from previous ions (σ_{cs/cs_1}). A similar behavior is assumed for the formation of an amorphous region, where the contributions from direct ion impacts (σ_{a/c_2}) and stimulated growth (σ_{as/cs_2}) are considered. With increasing fluence, the concentration of point defects and defect clusters will reach a saturation value, that is described by f_s.

In this work, we apply the above described model, which was developed to analyze the damage build-up derived by RBS/C, to the XRD measurements. If we analyze Figure 4, where the evolution of the maximum strain as a function of the fluence is shown, the presented model achieves a good fit of the experimental data. Since the XRD technique is not directly sensitive to amorphization, the second saturation level cannot be attributed to amorphous regions. Nevertheless, the results suggest that another type of defects is responsible for the increase of strain for the last three fluences. Thus, the creation of two different types of cluster, designated by clusters of type I and clusters of type II, are considered and described by the equations (2) and (3), respectively. Notice that the term cluster can range from aggregates of point defects, to dislocation loops and stacking faults [36]. Furthermore, it is possible that certain phases, such as amorphous regions or randomly distributed nanocrystals that do not strongly contribute to the diffraction pattern, influence the strain state of adjacent crystalline material. Figure 4 also shows the contributions of f_{pd}, f_{c/c_1} and f_{a/c_2}, represented by dash, dash-dot and dot lines, respectively. In addition, one should note that the two saturation levels, observed in figure 4, occurred in different depths (see Figure 3.(a)).

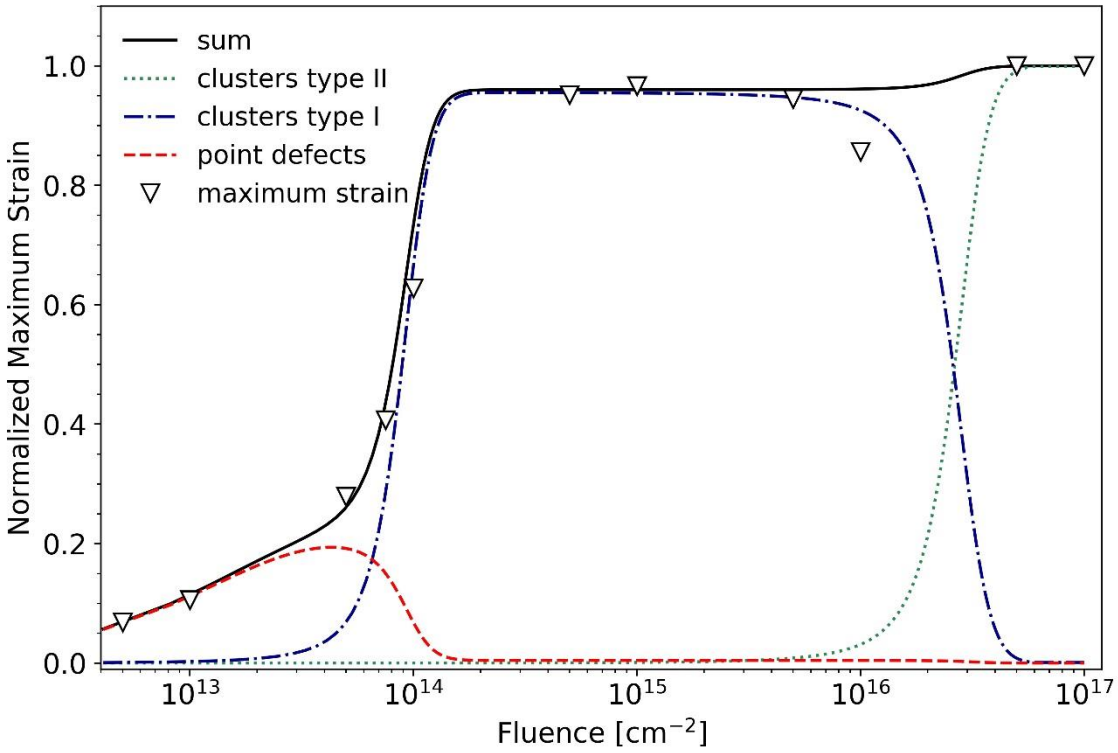

Figure 4 – Evolution of the maximum strain as a function of the fluence. The solid line is the fit of experimental data using the model described by Equation (1)-(5). The dash, dash-dot and dot lines represent the contributions of f_{pd}, f_{c/c_1} and f_{a/c_2} to the damage build-up, respectively.

In order to analyze the damage build-up in a fixed region, the same model was used to fit the experimental curves of the average strain (Figure 5), for the three regions indicated in Figure 3: region I (200-250 nm) corresponding to the depth of maximum nuclear energy deposition, region II (250-330 nm) with both high nuclear energy deposition and high concentration of implanted ions, and region III (330-425 nm) corresponding to the deeper region of the implanted layer with relatively low nuclear energy deposition. The fits obtained are shown in Figure 5 and the fitting parameters are summarized in Table 1. The evolution of the average static DW factor within each region is also shown. The number of displacements per atom (DPA) determined by SRIM simulation and corresponding to the maximum of the damage profile for each fluence are shown at the top of Figure 5. The uncertainties associated with each average strain value were estimated by uniformly changing the entire strain profile until the respective simulated diffractogram would no longer lead to any acceptable fit. This procedure allows to obtain two extreme values for the average strain in each region as represented by the error bars in Figure 5. The same method was applied to obtain the error bars relative to the average static DW factor values. A similar procedure but changing strain and DW factors solely in each region of interest (regions I, II and III in Figure 3) led to similar uncertainties.

Furthermore, one must keep in mind two considerations. Firstly, for regions with DW factors below ~0.06, the strain values do not have a significant influence on the simulated

diffractogram and uncertainties are very high. Moreover, for regions with a strain value below 0.1% (corresponding to a normalized strain of about 0.037) any change in the static DW factor does not produce a visible effect in the simulation, since this effect is masked by the signal coming from deeper undamaged regions. In these two situations, the average values of the strain and the static DW factor become meaningless. Thus, in Figure 5, these points are crossed out.

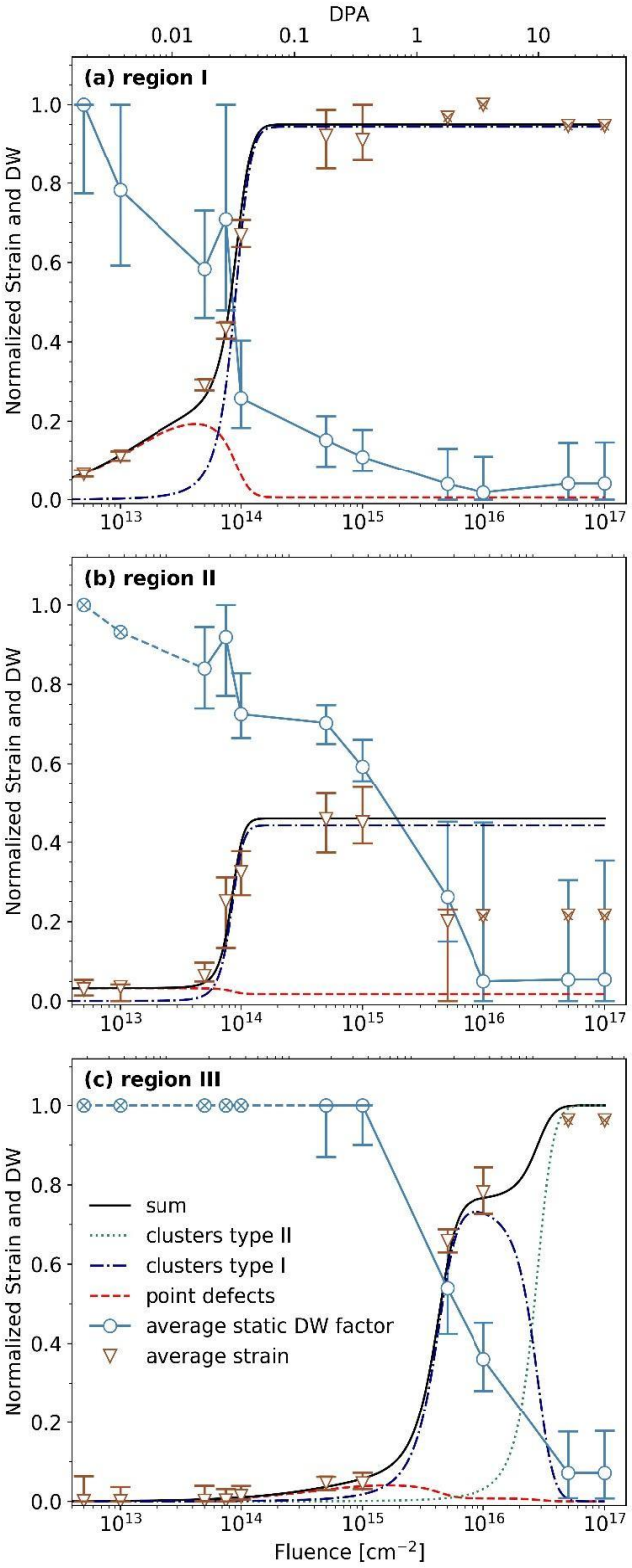

Figure 5 – Evolution of the average strain and static DW factor in (a) region I, (b) region II and (c) region III. The fits of experimental data using the model described by Equations (1)-(5) are represented by solid lines. The contributions of f_{pd}, f_{c/c_1} and f_{a/c_2} are shown by the dash, dash-dot and dot lines, respectively. The DPA values are also shown at the top of the graph. Symbols which are crossed out correspond to values with too high experimental uncertainties (see text).

All the fits presented in Figure 5 demonstrate a very close agreement with the experimental data. It is clear that the evolution of strain depends on the region considered. In region I (Figure 5.(a)), a gradual increase of the strain is accompanied by a gradual decrease of average static DW factor for fluences below 7.5×10^{13} cm^{-2}, which is predominantly attributed to the formation of point defects. When the fluence increases further, the fraction of clusters of type I becomes higher than the fraction of point defects, giving rise to a significant increase of strain and damage (decrease in the average static DW factor) in this region. A similar behavior is observed in Figure 5.(b), corresponding to region II, however, the saturation level following the strong increase in strain due to clusters of type I is different in the two regions. The negligible changes in the diffractograms for the fluences of 5×10^{14} cm^{-2} and 1×10^{15} cm^{-2}, are consistent with the strain saturation in regions I and II, while strain in region III is still insignificant (Figure 5.(c)). The drastic change of the response of the material to further defect formation in this regime, together with the significant increase of the damage (with static DW factors below 0.2 in region I) corroborate the assumption made above that, once the strain induced by point defects and defect clusters reaches a threshold value supported by the material, a morphological alteration of these defects to extended defects can occur, to minimize the strain inside the crystal. Thus, stacking faults and dislocation loops may be formed, and consequently a saturation of the strain is observed – Figure 5.(a) and 5.(b). Amorphization in MoO_3, on the other hand, was only reported for much higher fluences at DPA values above 3 [16].

In region II (Figure 5.(b)), a decrease of the average strain occurs at fluence 5×10^{15} cm^{-2}, accompanied by a decrease of the static DW factor. In fact, the formation of extended defects such as stacking faults and dislocation loops can be considered as a mechanism of the lattice minimizing the strain induced by point defects and defect clusters, as it was also observed in studies of Si [37] and SiGe alloys [38,39]. Furthermore, a recent work combining XRD and computational modelling revealed a general strain accumulation and relaxation mechanism common in several distinct oxide crystals, where strain accumulation induced by interstitial point defects and dislocation loops is followed by a strain relaxation when dislocation loops interact to form a network of dislocation lines [33]. The DPA values at which relaxation occurs depend on the material and radiation conditions, but some representative values found in the literature are around 6-7 DPA for UO_2 implanted at room temperature and cubic ZrO_2 implanted at 80 K, and around 0.1-0.2 DPA for MgO implanted at 573 K [33]. For comparison, in the present case a strain relaxation occurs in region II for DPA between 0.2 and 1.

Above 1×10^{16} cm^{-2} (DPA>3.8), the static DW factor in the implanted layer is very close to 0 which indicates that these regions are highly damaged. Indeed, this behavior is in agreement with previous studies in MoO_3 implanted with Kr, where a gradual amorphization of the implanted layer was verified for DPA values between ~3.3 and ~33, using electron diffraction measurements[16].

In region III (Figure 5.(c)), only a slight increase of strain due to the existence of point defects is observed for fluences below 1×10^{15} cm^{-2}. This is expected since the nuclear energy deposition, i.e. the local fluence, in this region is very low. Above 1×10^{15} cm^{-2}, the fraction of defect clusters becomes dominant and causes a rapid increase of the strain in the lattice. On the other hand, according to the SRIM simulation (Figure 3.(c)), the concentration of primary defects is very low in region III. Thus, it is safe to assume that the increase of strain in this region results from defect migration from the region of maximum nuclear interaction to deeper regions of the sample where they seem to accumulate.

In contrast to the behavior in regions I and II, in region III after the saturation of clusters of type I at a fluence around 1×10^{16} cm^{-2}, the strain appears to increase again. However, it should be kept in mind that at these high fluences the static DW factors approach zero in almost the entire implanted volume, meaning that the sensitivity of XRD to strain is strongly reduced. Although the average strain cannot be evaluated for fluence values above 5×10^{16} cm^{-2} due to low DW factors in part of region III, analyzing figures 3.(a) and 3.(b), the behavior becomes clearer. Indeed, a new increase of strain followed by a second saturation is observed at depths greater than 400 nm, where the static DW factor values remain sufficiently high. This additional step of strain increase is attributed to the formation of a different kind of defect clusters (type II in the fitting model) and may be related to the on-set of amorphization in region I. Gradual amorphization is expected to occur between ~3.3 and ~33 DPA [16] and may alter the defect migration mechanisms. Moreover, the clusters formed in region III are possibly different from those created in regions I and II, since there is a lack of direct nuclear energy deposition in region III when compared to regions I and II. In fact, the migration of point defects to deeper regions and the formation of large defect clusters beyond the implanted layer were also observed in GaN [27]. In this semiconductor, based on transmission electron microscopy (TEM) images, it was observed that in regions without direct displacements of the lattice atoms due to the collision cascade, there was no formation of stacking faults, which favors the formation of large defect clusters and prevents the minimization of the strain [27]. At this stage it is not possible to infer on the exact nature of the distinct extended defects formed in MoO_3. Unfortunately, TEM analysis in MoO_3 is very challenging due to the brittle nature of the crystals and the sensitivity of the material to the electron beam.

Comparing the parameters presented in Table 1, some further conclusions can be made. The cross section for recombination of point defects is always higher than the cross section for point defect formation. Furthermore, the stimulated growth of clusters of type I/II is always more favorable than the creation of clusters by direct ion impact. Such behaviors demonstrate that the defects created by implantation are highly mobile which favors their recombination as well as the interaction between defects in agreement with the various defect transformations described above. If we analyze the region where the interaction with the incident ion beam is the highest (region I), it is also verified that the cross section for the formation of point defects (Table 1) is about two orders of magnitude

higher than that obtained by SRIM calculations ($\sigma_{SRIM} = 4\times10^{-16}$ cm^{-2})[1]. This fact suggests that the damage observed by the XRD measurements does not come solely from the nuclear interaction between the implanted oxygen ions and the atoms of the lattice, but that there are some other processes involved. Indeed, the electronic interaction processes can introduce damage in the lattice by creating vacancies in MoO_3 via radiolysis, as previously reported [17]. Thus, a similar process may occur in the present samples, contributing to the increase of strain in particular in regions close to the surface where electronic interaction is higher.

Table 1 - Summary of the parameters obtained by fitting the experimental data in Figure 5, using the model described for Equation (1)-(5): σ_{pd}, σ_{c/c_1} and σ_{a/c_2}, the cross sections for the formation of point defects, defect clusters of type I and type II, respectively; σ_r the cross section for point defect recombination; σ_{cs/cs_1} and σ_{as/cs_2}, the cross sections for stimulated growth of defect clusters of type I and type II, respectively; and f_s, the defect cluster saturation concentration.

	Region I	**Region II**	**Region III**
$\boldsymbol{\sigma_{pd}}$ **(10^{-14} cm^2)**	1.6	5	0.01
$\boldsymbol{\sigma_r}$ **(10^{-14} cm^2)**	6	150	0.22
$\boldsymbol{\sigma_{c/c_1}}$ **(10^{-16} cm^2)**	1.9	0.1	0.1
$\boldsymbol{\sigma_{cs/cs_1}}$ **(10^{-14} cm^2)**	8.5	11	0.12
$\boldsymbol{f_s}$	0.95	0.46	0.76
$\boldsymbol{\sigma_{a/c_2}}$ **(10^{-16} cm^2)**	-	-	0.01
$\boldsymbol{\sigma_{as/cs_2}}$ **(10^{-16} cm^2)**	-	-	2

3.2. Micro-Raman spectroscopy

Although no additional peaks were observed for implanted samples in 2θ-θ XRD scans between 10 and 90 degrees (not shown), we cannot exclude the formation of some inclusions of different phases, with reduced volume and crystalline quality, and therefore, not visible in the XRD measurements. To detect such minority phases micro-Raman measurements were carried out in smooth areas of the oxygen-implanted samples, as shown in Figure 6. A Raman spectrum of an as-grown (not implanted) crystal, recorded in the same experimental conditions, is included for comparison.

[1] σ_{SRIM} was obtained by N_{displ}/N, where N_{displ} is the number of displacements per incident ion and unit depth in the maximum of displacement profile and N is the atomic density of MoO_3.

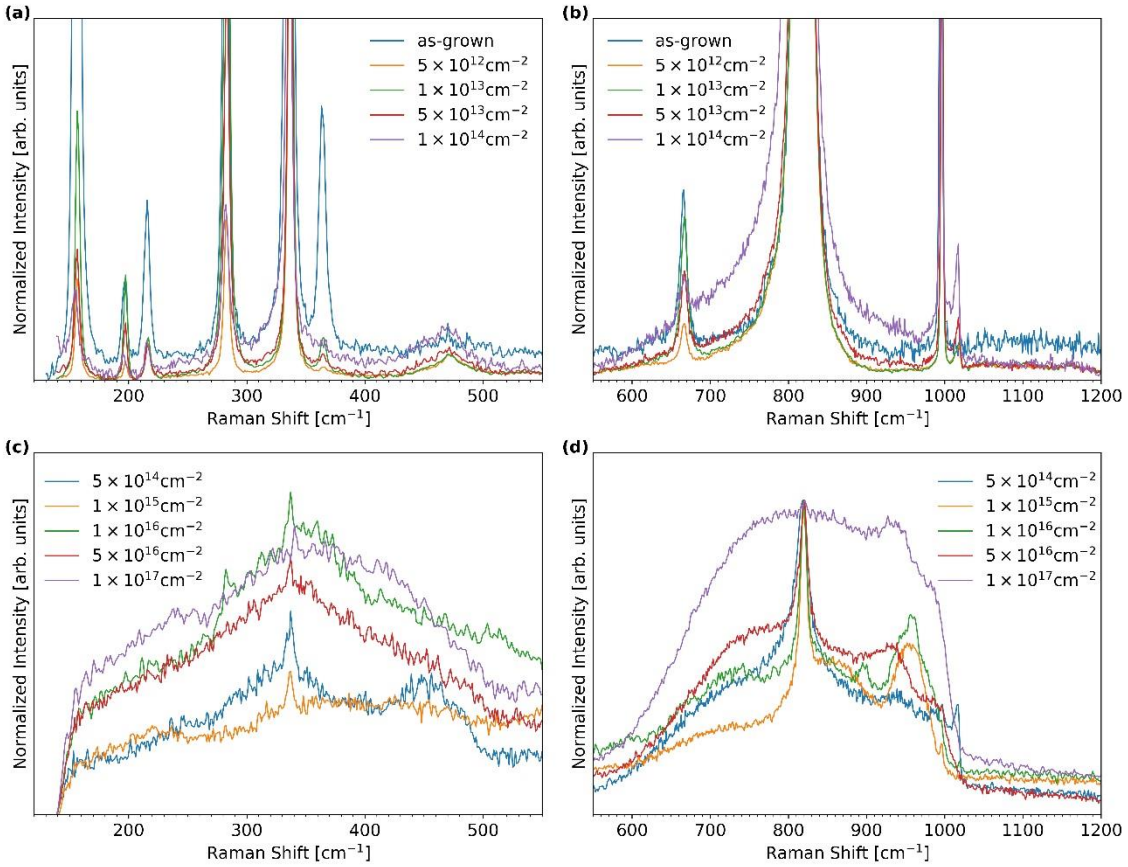

Figure 6 - Normalized Raman spectra of the oxygen implanted MoO_3 samples. The frequency range has been divided in two intervals for better visualization (a,c) from 120 to 550 cm^{-1} and (b,d) from 550 to 1200 cm^{-1}. (a) and (b) show spectra for fluences 5×10^{12} - 1×10^{14} cm^{-2}. (c) and (d) show spectra for fluences 5×10^{14} - 1×10^{17} cm^{-2}. A Raman spectrum of an as-grown sample is included for comparison.

Up to a fluence of about 5×10^{13} cm^{-2}, Raman spectra of the implanted samples are rather similar - in terms of peak positions, bandwidths and phase purity - to that corresponding to the α-MoO_3 as-grown material. For those samples, Raman peaks appear centered at about 1018, 997, 820, 667, 472, 364, 337, 283, 217, 197, 157 cm^{-1}, which are characteristic of the orthorhombic α-MoO_3 structure [11,40–42]. In fact, the simulations of strain accumulation – Figure 5 – suggest that point defect recombination is high ($\sigma_r > \sigma_{pd}$), which may give rise to a low concentration of oxygen vacancies. Nevertheless, careful comparison of the spectrum for fluence 5×10^{13} cm^{-2} with that of the as-grown sample reveals small changes in the oxygen stoichiometry. Namely, oxygen deficiency in α-MoO_3 broadens the bands at 820 and 996 cm^{-1} [11]. Moreover, anion deficiency induces additional Raman bands in the (1005 – 1020) cm^{-1} range related to the stretching vibrations of a newly formed terminal Mo=O bond in the *b*-direction of the MoO_4 tetrahedral structural units [11]. Such changes are clearly noticeable for implantation fluences above 5×10^{13} cm^{-2}. For fluences equal to or higher than 5×10^{14} cm^{-2}, Raman spectra reveal the formation of molybdenum oxide minority phases different from α-MoO_3, as revealed by the appearance of new Raman bands in the range of (850 – 1000) cm^{-1}. In several cases, Raman bands are too broad or weak to clearly ascertain their origin.

The peak positions of all the Raman bands observed in Figure 6 are summarized in Table 2, together with their corresponding assignments [11,12,48,40–47]. Rather than to MoO_2 or other MoO_3 phases, such as h-MoO_3 or β-MoO_3, the Raman bands found for intermediate and high fluences mainly correspond to the so-called Magnéli phases, defined by the general formula Mo_nO_{3n-1} (Mo_4O_{11}, Mo_5O_{14}, Mo_8O_{23}). These compounds result from accommodation of oxygen deficiency through the formation of different types of crystallographic shear planes [49,50] and their physical properties are unknown to a great extent. In fact, the removal of oxygen from MoO_3 may lead to ordered crystallographic shear structures via extended shear, thus destroying the translational symmetry [49–51]. On the other hand, it is important to mention that the formation mechanisms of shear structures often involves extended defects such as dislocation loops and stacking faults and, in some models, vacancy loops limited by partial dislocations [52]. The increased bandwidth of the Raman peaks and the broad background observed in the spectra of crystals implanted with higher fluences probably arise from a combination of a multitude of acoustic and acoustic plus optical modes due to a relaxation of the *k*-selection rules, indicative of a change in the crystallinity of the implanted samples.

Table 2 – Raman peak positions observed in Figure 6 and their corresponding phase assignments.

Fluence [cm^{-2}]	**Raman peak positions [cm^{-1}]**	**Phase**
As-grown	995, 819, 666, 363, 336, 282, 216, 196, 156	α - MoO_3[11,40–43]
5×10^{12}	1018, 997, 820, 667,472, 364, 337, 283, 217, 197, 157	α - MoO_3[11,40–43]
1×10^{13}	1018, 997, 820, 667,470, 364, 337, 283, 217, 197, 157	α - MoO_3[11,40–43]
5×10^{13}	1017, 996, 820, 667,471, 364, 337, 283, 216, 197, 157	α - MoO_3[11,40–43]
1×10^{14}	1016, 995, 819, 666, 465, 336, 282, 216, 195, 155	α - MoO_3[11,40–43]
5×10^{14}	1017, 997, 820, 337 ~939 ~448	α - MoO_3[11,40–43] Mo_8O_{23}[48,53,54] Mo_4O_{11}[12,45,54]

1×10^{15}	995, 821, 337 954, ~725 857	α - MoO_3[11,40–43] Mo_8O_{23}[48,53,54] β-MoO_3[41]
1×10^{16}	984, 895 959, 937 821, 337, 282 742	Mo_4O_{11}[12,45,54] Mo_8O_{23}[48,53,54] α - MoO_3[11,40–43] MoO_2[11,44,46,47]
5×10^{16}	978, 930 820, 337	Mo_8O_{23}[48,53,54] α - MoO_3[11,40–43]
1×10^{17}	927 821, 340	Mo_8O_{23}[48,53,54] α - MoO_3[11,40–43]

3.3. Electrical Characterization

To evaluate the influence of the structural changes induced by implantation on the electrical properties of the MoO_3 lamellar crystals, I-V curves were measured and a few selected curves are shown in Figure 7.(a) and 7.(b). For as-grown samples and fluences below 1×10^{15} cm^{-2} the devices present high resistivity, in fact too high to be measured in our equipment. For fluences above 1×10^{15} cm^{-2}, an increase in conductivity is observed with increasing fluence, leading to an increase of the measured current values from microamperes to milliamperes.

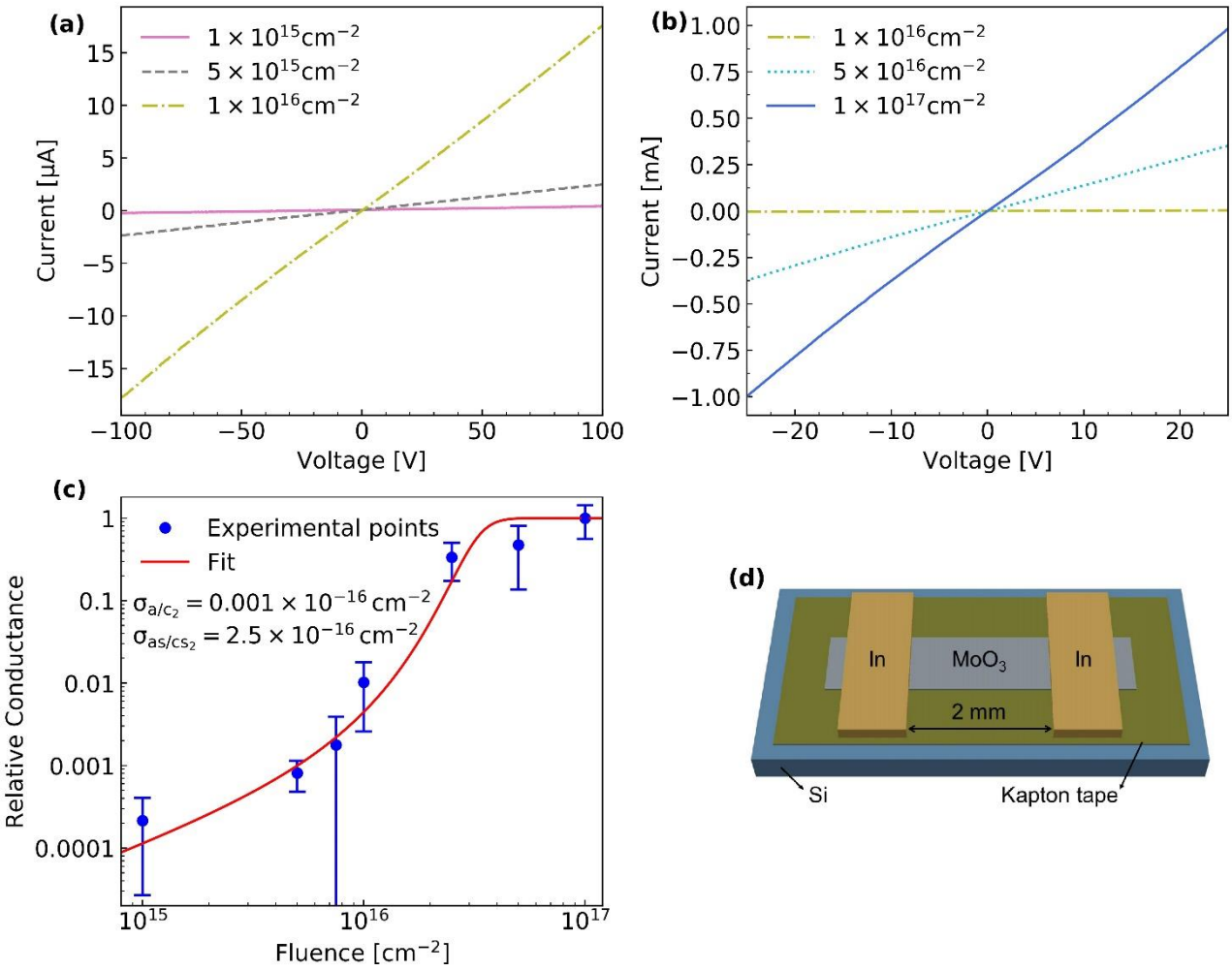

Figure 7 – Evolution of the IV-curves with increasing fluence: (a) fluence range from 1×10^{15} cm^{-2} to 1×10^{16} cm^{-2}; (b) fluence range from 1×10^{16} cm^{-2} to 1×10^{17} cm^{-2}. Note the different current and voltage scales in Figure 7.(a) and (b). A current limit of 1 mA was chosen to protect the devices. (c) Evolution of the relative conductance with increasing fluence. (d) Schematic illustration of the geometry of a MoO_3 lamellar crystal device used for electrical characterization.

Assuming that the contact resistance and width of the conductive channel caused by the implantation do not change with the fluence, the decrease of the total electrical resistance (increase of the total electrical conductance) can be directly assigned to the increase of conductivity of the ion implanted layer. Thus, as a measure for the electrically detected lattice damage, we define the relative change of the conductance (s):

$$s = \frac{G}{G_{max}} = \frac{R_{max}}{R} \tag{6}$$

With G the conductance for each fluence, G_{max} the maximum measured conductance, R the resistance for each fluence and R_{max} the maximum measured resistance.

Figure 7.(c) shows the evolution of the relative conductance with increasing fluence. A total increase of conductance of about four orders of magnitude is observed. The presented values correspond to averages measuring several devices implanted to the same fluence. The relatively large error bars reflect some challenges in device processing. Indeed, we do not have a strict control of the lateral dimensions and thicknesses of the crystals as well as the homogeneity of the contacts on the brittle surface. Nevertheless, regardless of these issues, a clear tendency of increase in conductance (decrease in resistance) with increasing fluence is verified which enables tuning of the electrical properties of the material.

It is important to mention, that the gain in conductivity is more stable than what was observed for annealing treatment in vacuum of the same material [20]. For example, after 7 days of exposure to air, the conductance of an annealed sample decreases to only 1.3% of its initial value, thus approaching the limits of the equipment. On the contrary, the conductance of the implanted samples only decreased to 65% of its initial value, after 9 days of exposure to air.

Comparing the evolution of the relative conductance with the strain build-up in the different regions of the samples – Figure 5 – the increase in conductance observed for fluences above $1 \times 10^{-15} cm^2$ seems to be related with the evolution of strain in region III, and may therefore be correlated with the formation of defect clusters in this region and/or the amorphization of the crystal in region I. As mentioned before, Naguib *et al.* [16] observed a gradual increase of sheet conductivity of MoO_3 implanted with Kr for DPA values between ~3.3 and ~33 (corresponding to oxygen fluences from 8.5×10^{15} cm^{-2} to 8.5×10^{16} cm^{-2} for our implantation conditions), which was attributed to a gradual amorphization of the implanted layer. Indeed, applying Equation (5), which is often used to model amorphization of crystals upon ion implantation [55], a good fit was obtained as shown by the red line in Figure 7.(c). As mentioned above it is likely that the on-set of amorphization in region I leads to the enhanced defect migration to deeper layers and the increase of defect clusters in region III.

Comparing the fit parameters for the electrical measurements – given in Figure 7.(c) – with those for the XRD measurements (Table 1) it is possible to conclude that the obtained cross section for stimulated growth of defect clusters of type II/amorphized material ($2.5 \times 10^{-16} cm^2$) is very similar to that obtained from the simulation of the average strain profile in region III ($2 \times 10^{-16} cm^2$). Furthermore, the cross section of stimulated growth ($2.5 \times 10^{-16} cm^2$) is substantially higher than the cross section for formation of clusters of type II/amorphization by direct impact ($0.001 \times 10^{-16} cm^2$), again in agreement with the XRD results. These similarities between the evolution of conductivity and the damage build-up in region III suggests again that the increase of conductance is related to highly damaged regions containing extended defects and/or amorphous zones.

4. Discussion

The strong increase (over several orders of magnitude) of conductivity of MoO_3 upon ion implantation is remarkable. In fact, in most semiconductors, defects produced by ion implantation create deep levels in the band gap which reduce the conductivity [56]. In contrast, an increase of electrical conductivity upon ion implantation was reported in In_2O_3 and attributed to the formation of large defect complexes that behave like donor defects [57].

There is a clear experimental evidence that oxygen vacancies increase the electrical conductivity of α-MoO_3 [17,56], due to the formation of shallow donor levels [11,58,59]. Furthermore, high electron mobilities were reported for partially reduced MoO_3 [60]. Such conductivity increase is for example observed in our samples upon annealing in vacuum [20]. Similar to our results, Hanson *et al.*[17] observed an exponential decay in resistance, of about four orders of magnitude, as a function of the dose in MoO_3 nanosheets with different thicknesses when irradiated with an electron beam. Based on electron energy loss spectroscopy and Raman spectroscopy, this behavior was attributed to the increase of free carrier concentration resulting from the formation of oxygen vacancies by reduction of the MoO_3 via radiolysis [17]. Moreover, H. M. Naguib *et al.*[16] also reported an exponential increase in the sheet conductivity of MoO_3 implanted with Kr ions, as a function of fluence. This behavior was explained by the amorphization of the implanted layer, followed by recrystallization in the more conductive MoO_2 phase, as demonstrated by reflection high energy electron diffraction measurements [16]. This phase change was accompanied by a color change of the MoO_3 material. In contrast, in the present study no MoO_2 phase and no color change was observed.

Ion implantation will induce a large quantity of oxygen vacancies, as seen in Figure 3.(c). For example, for a fluence of 5×10^{14} cm^{-2}, an appreciable concentration of 10^{22} O vacancies.cm^{-3} in the peak of the defect profile is expected. Indeed, for a fluence of 1×10^{14} cm^{-2} the signature of oxygen vacancies is clearly observed in the Raman spectra (Figure 6). Nevertheless, the samples remain highly resistive for fluences below 1×10^{15} cm^{-2}. Actually, this is not surprising since oxygen vacancies and interstitials are always created in pairs and O interstitials should act as acceptors compensating the V_O donors. A similar reasoning applies for Mo vacancies and interstitials. Unpaired oxygen vacancies would only be formed if oxygen is expelled from the surface, as proposed by Hanson *et al.*[17] for electron irradiation of few layer MoO_3, or if it is intercalated, possibly as O_2, in the Van der Waals gap. The high mobility of the defects formed can also favor their mutual interaction and subsequent recombination processes, leading to a decrease in the concentration of oxygen vacancies.

On the other hand, the stepwise increase of strain in the implanted region - Figure 3 - reveals the formation of stable defects (besides point defects probably small clusters or dislocation loops are formed as observed for many materials[26–29,33]). The first significant increase of conductivity occurs for a fluence of 1×10^{15} cm^{-2}, which

corresponds to the range of fluences where a saturation of perpendicular strain is verified by HRXRD measurements. According to the used model, this behavior suggests that the decrease of resistivity may result from highly damaged regions, probably associated with the creation of extended defects, in accordance with the model proposed for In_2O_3 [57]. The creation of amorphous regions may also contribute to the decrease of resistivity for high fluences, as observed in Kr-irradiated MoO_3 sheets for DPA>3 which corresponds to an O-fluence of 1×10^{16} cm^{-2} under the present implantation conditions [16]. At the same time, the appearance of new minority phases with O/Mo ratio between two and three (2<O/Mo<3), revealed by micro-Raman spectroscopy for fluences of 5×10^{14} cm^{-2} and above, might also induce an increased electrical conductivity in the implanted samples. In fact, Bando *et al.*[61] reported on the conductivity of Mo_nO_{3n-1} (n = 4,8,9) crystals. Except triclinic Mo_9O_{26}, which showed a semiconductor behavior, the other intermediate oxides were found to exhibit metallic conductivity attending to both the value and the temperature dependence of resistivity. In addition to the formation of oxygen vacancies and minority phases, the effect of uniaxial strain on the band diagram of MoO_3 should be studied in the future, similar to ion beam strain engineering of the band gap reported for WO_3[18].

Finally, it is worth to note that the conductivity induced by ion implantation is stable during days, relatively to as-implanted samples. Indeed, samples annealed in vacuum reveal an unstable gain in conductivity which decreases significantly when storing the sample in air during few days [20].

Concerning the change of the structural properties of the MoO_3 crystals upon ion implantation, the complex strain build-up and relaxation processes described above deserve some further discussion. Based on the strain and damage profiles obtained by XRD, an increase of the maximum perpendicular strain in several steps is observed. In particular, two fluence regions of strain saturation are observed with different saturation levels and attributed to different depths of the implanted layer. The first saturation occurs in a region of high nuclear interaction, probably resulting from a morphological alteration of the defect structure. A recent study combining XRD with molecular dynamics and rate equation cluster dynamics simulations attributes strain build-up and subsequent relaxation in several distinct crystals (namely UO_2, ZrO_2, MgO and ZrC) to a common mechanism [33]. These authors attribute the initial strain increase to the clustering of interstitial defects into dislocation loops, while the strain relaxation at higher fluences is explained by the joining of individual dislocation loops into a network of dislocation lines. A similar rearrangement of defects is clearly observed in MoO_3 for intermediate fluences. However, in contrast to these studies, when the fluence is further increased, the maximum strain in the deep region III increases to even higher values than the first saturation level, followed by a second saturation. These results suggest that a migration of the defects occurs from region I/II towards deeper regions. Interestingly, the strain values supported by the lattice (up to 3%) are higher compared to other materials, where similar transformations are reported for strain levels below 2% [27,30,33,34]. In the

absence of further microstructural information on the nature of defects that are formed, we attribute the pronounced differences observed for MoO_3 to the layered crystal structure. In many layered 2D crystals high expansions of the Van der Waals gap have been reported when impurity atoms or molecules are intercalated between the 2D crystal layers, which are only weakly bound by Van der Waals forces [62]. Although in the present study no impurities are introduced, it is safe to assume that a large number of the produced interstitials will arrange within this region in MoO_3. This rearrangement, leads to the observed large expansion along the *b*-direction without strongly affecting the remaining crystal structure. On the other hand, it was shown that high concentrations of isolated oxygen vacancies are not stable in MoO_3 and that the formation of intermediate phases with a ratio of O/Mo <3 is energetically favorable [63]. Indeed, our data suggest that O/Mo <3 Magnéli phases are formed in the fluence region where the first strain saturation occurs. In particular, Raman spectra show peaks attributed to the Mo_8O_{23} and Mo_4O_{11} phases, which possess non-layered crystal structures with 3D bonding scheme, as well as peaks of the $Mo_{18}O_{52}$ phase which has a layered structure like MoO_3. These "suboxide" phases also occur during partial reduction of MoO_3 [63]. Regarding our results, these suboxide phases are first observed in the fluence range corresponding to the first strain relaxation and probably contribute to this strain saturation. In fact, phase changes upon ion implantation have been observed in other oxides such as Gd_2O_3 and Ga_2O_3 [64,65]. When region I and II become saturated with extended defects including suboxide phases, defects start to migrate towards deeper regions. It is reasonable to assume that interstitials are more mobile than vacancies, as typically observed in oxides [57]. They will intercalate in the Van der Waals gap in the deeper less damaged region of the implanted crystal. Since primary defect formation is low in this region, vacancy concentration will be low, and the phase transitions and relaxation set in at slightly higher strain levels than observed for region II. Transmission electron microscopy (TEM) analysis of implanted samples would be highly desirable to corroborate this model. However, sample preparation is challenging due to the brittle nature of the used lamellar crystals. On the other hand, the MoO_3 is quite sensitive to electron beam irradiation in the TEM, which may originate damage and structural changes within the first few minutes. In fact, the MoO_3 reduction by radiolysis and heating [17,50] and the crystallization of amorphous regions [66] have been reported as consequences of MoO_3 exposure to the electron beam in a TEM. Unfortunately, due to the high relative tilt of the 2D lamellas, ion channeling measurements, which would provide a direct measurement of displaced atoms, were not possible to perform.

5. Conclusions

In this work, α-MoO_3 lamellar crystals were implanted with oxygen ions in a wide fluence range. A remarkable increase of the conductivity over several orders of magnitude was induced by high fluence ion implantation and attributed mainly to the formation of extended defects and partial amorphization as well as the formation of new suboxide minority phases with O/Mo ratios between two and three. On the other hand, simple point defects created by the implantation, such as Frenkel pairs, do not seem to contribute significantly to the conductivity increase. The possibility to tune the electrical properties of MoO_3 by ion implantation holds a considerable potential for novel device designs enabling, for example, the definition of buried conductive paths. However, further studies are necessary to assess the stability of the conductivity upon annealing at typical device processing temperatures. Additionally, the comprehensive XRD study revealed further exceptional properties of MoO_3. In particular, the strain induced by ion implantation with a maximum deformation of approximately 3% along the *b*-direction of the crystal is higher than that typically measured in ion implanted oxide crystals and may be the driving force for the strong migration of defects found to occur during ion implantation. Possibly, this is due to the typical layered structure of MoO_3, which allows the accommodation of defects in the so-called Van der Waals gap without leading to a break-down of crystalline order. In fact, Raman peaks of the α-phase are dominant up to the highest fluence.

Acknowledgements

This work was supported by the Fundação para a Ciência e a Tecnologia (FCT) [grants PTDC/CTM-CTM/28011/2017, LISBOA-01-0145-FEDER-028011, CERN/FIS/NUC/0004/2015, UID/FIS/50010/2013, UID/Multi/04349/2013, SFRH/BPD/111285/2015 and Investigador FCT] as well as by project MAT2015-65274-R (MINECO / FEDER).

References

[1] I.A. de Castro, R.S. Datta, J.Z. Ou, A. Castellanos-Gomez, S. Sriram, T. Daeneke, K. Kalantar-zadeh, Molybdenum Oxides – From Fundamentals to Functionality, Adv. Mater. 29 (2017) 1–31.

[2] S. Balendhran, S. Walia, M. Alsaif, E.P. Nguyen, J.Z. Ou, S. Zhuiykov, S. Sriram, M. Bhaskaran, K. Kalantar-zadeh, Field Effect Biosensing Platform Based on 2D a-MoO3, ACS Nano. 7 (2013) 9753–9760.

[3] S. Bai, C. Chen, D. Zhang, R. Luo, D. Li, A. Chen, C.-C. Liu, Intrinsic characteristic and mechanism in enhancing H2S sensing of Cd-doped a-MoO3 nanobelts, Sensors Actuators B Chem. 204 (2014) 754–762.

[4] H.-Y. Chen, H.-C. Su, C.-H. Chen, K.-L. Liu, C.-M. Tsai, S.-J. Yen, T.-R. Yew,

Indium-doped molybdenum oxide as a new p-type transparent conductive oxide, J. Mater. Chem. 21 (2011) 5745–5752.

[5] X. Hu, W. Zhang, X. Liu, Y. Mei, Y. Huang, Nanostructured Mo-based electrode materials for electrochemical energy storage, Chem. Soc. Rev. 44 (2015) 2376–2404.

[6] R.K. Sharma, G.B. Reddy, Controlled growth of vertically aligned MoO3 nanoflakes by plasma assisted paste sublimation process, J. Appl. Phys. 114 (2013) 184310.

[7] H. Sitepu, Texture ans structural refinement using neutron diffraction data from molybdite (MoO3) and calcite(CaCO3) powders and a Ni-rich Ni50.7Ti49.30 alloy, Powder Diffr. 24 (2009) 315–326.

[8] D.O. Scanlon, G.W. Watson, D.J. Payne, G.R. Atkinson, R.G. Egdell, D.S.L. Law, Theoretical and Experimental Study of the Electronic Structures of MoO3 and MoO2, J. Phys. Chem. C. 114 (2010) 4636–4645.

[9] M. Vasilopoulou, A.M. Douvas, D.G. Georgiadou, L.C. Palilis, S. Kennou, L. Sygellou, A. Soultati, I. Kostis, G. Papadimitropoulos, D. Davazoglou, P. Argitis, The Influence of Hydrogenation and Oxygen Vacancies on Molybdenum Oxides Work Function and Gap States for Application in Organic Optoelectronics, J. Am. Chem. Soc. 134 (2012) 16178–16187.

[10] K.W. Harrison, C.D. Corolewski, M.D. Mccluskey, J. Lindemuth, S. Ha, M.G. Norton, M.G. Norton, Electronic transport in molybdenum dioxide thin films, J. Mater. Sci. Mater. Electron. 26 (2015) 9717–9720.

[11] M. Dieterle, G. Weinberg, G. Mestl, Raman spectroscopy of molybdenum oxides. Part I. Structural characterization of oxygen defects in MoO3-x by DR UV/VIS, Raman spectroscopy and X-ray diffraction, Phys. Chem. Chem. Phys. 4 (2002) 812–821.

[12] M. Dieterle, G. Mestl, Raman spectroscopy of molybdenum oxides. Part II. Resonance Raman spectroscopic characterization of the molybdenum oxides Mo4O11 and MoO2, Phys. Chem. Chem. Phys. 4 (2002) 822–826.

[13] A. Borgschulte, O. Sambalova, R. Delmelle, S. Jenatsch, R. Hany, F. Nüesch, Hydrogen reduction of molybdenum oxide at room temperature, Sci. Rep. 7 (2017) 40761.

[14] J.Z. Ou, J.L. Campbell, D. Yao, W. Wlodarski, K. Kalantar-zadeh, In Situ Raman Spectroscopy of H2 Gas Interaction with Layered MoO3, J. Phys. Chem. C. 115 (2011) 10757–10763.

[15] M. Vila, C. Díaz-Guerra, D. Jerez, K. Lorenz, J. Piqueras, E. Alves, Intense

luminescence emission from rare-earth-doped MoO3 nanoplates and lamellar crystals for optoelectronic, J. Phys. D. Appl. Phys. 47 (2014) 355105.

[16] H.M. Naguibt, R. Kelly, On the increase in the electrical conductivity of MoO3 and V2O5 following ion bombardment, J. Phys. Chem. Solids. 33 (1972) 1751–1759.

[17] E.D. Hanson, L. Lajaunie, S. Hao, B.D. Myers, F. Shi, A.A. Murthy, C. Wolverton, R. Arenal, V.P. Dravid, Systematic Study of Oxygen Vacancy Tunable Transport Properties of Few-Layer MoO3−x Enabled by Vapor-Based Synthesis, Adv. Funct. Mater. 27 (2017) 1605380.

[18] A. Herklotz, S.F. Rus, S. KC, V.R. Cooper, A. Huon, E.-J. Guo, T.Z. Ward, Symmetry driven control of optical properties in WO3 films, APL Mater. 5 (2017) 066106.

[19] H. Guo, S. Dong, P. D.Rack, J. D.Budai, C. Beekman, Z. Gai, W. Siemons, C.M. Gonzalez, R. Timilsina, A.T. Wong, A. Herklotz, P.C. Snijders, E. Dagotto, T.Z. Ward, Strain Doping: Reversible Single-Axis Control of a Complex Oxide Lattice via Helium Implantation, Phys. Rev. Lett. 114 (2015) 256801.

[20] D.R. Pereira, M. Peres, L.C. Alves, J.G. Correia, C. Díaz-Guerra, A.G. Silva, E. Alves, K. Lorenz, Electrical characterization of molybdenum oxide lamellar crystals irradiated with UV light and proton beams, Surf. Coatings Technol. 355 (2018) 50–54.

[21] H.C. Zeng, Vapour phase growth of orthorhombic molybdenum trioxide crystals at normal pressure of purified air, J. Cryst. Growth. 186 (1998) 393–402.

[22] B. Yan, Z. Zheng, J. Zhang, H. Gong, Z. Shen, W. Huang, T. Yu, Orientation controllable growth of MoO3 nanoflakes: Micro-raman, field emission, and birefringence properties, J. Phys. Chem. C. 113 (2009) 20259–20263.

[23] M. Souilah, A. Boulle, A. Debelle, RaDMaX: A graphical program for the determination of strain and damage profiles in irradiated crystals, J. Appl. Crystallogr. 49 (2016) 311–316.

[24] A. Boulle, R. Guinebretière, A. Dauger, Phenomenological analysis of heterogeneous strain fields in epitaxial thin films using x-ray scattering, J. Phys. D. Appl. Phys. 38 (2005) 3907–3920.

[25] J.F. Ziegler, J.P. Biersack, U. Littmark, The Stopping and Range of Ions in Solids, Pergamon, New York, 1988.

[26] D.N. Faye, E. Wendler, M. Felizardo, S. Magalhães, E. Alves, F. Brunner, M. Weyers, K. Lorenz, Mechanisms of Implantation Damage Formation in AlxGa1-xN Compounds, J. Phys. Chem. C. 120 (2016) 7277–7283.

[27] B. Lacroix, S. Leclerc, A. Declémy, K. Lorenz, E. Alves, P. Ruterana, Mechanisms of damage formation in Eu-implanted GaN probed by X-ray diffraction, Europhys. Lett. 96 (2011) 46002.

[28] A. Debelle, J. Channagiri, L. Thomé, B. Décamps, A. Boulle, S. Moll, F. Garrido, M. Behar, J. Jagielski, Comprehensive study of the effect of the irradiation temperature on the behavior of cubic zirconia, J. Appl. Phys. 115 (2014) 183504.

[29] K. Lorenz, M. Peres, N. Franco, J.G. Marques, S.M.. Miranda, S. Magalhães, T. Monteiro, W. Wesch, E. Alves, E. Wendler, Radiation damage formation and annealing in GaN and ZnO, SPIE Conf. Proc. 7940 (2011) 249–250.

[30] A. Turos, P. Jóźwik, M. Wójcik, J. Gaca, R. Ratajczak, A. Stonert, Mechanism of damage buildup in ion bombarded ZnO, Acta Mater. 134 (2017) 249–256.

[31] E. Wendler, Mechanisms of damage formation in semiconductors, Nucl. Instruments Methods Phys. Res. Sect. B Beam Interact. with Mater. Atoms. 267 (2009) 2680–2689.

[32] N. Hecking, K.F. Heidemann, E. Te Kaat, Model of temperature dependent defect interaction and amorphization in crystalline silicon during ion irradiation, Nucl. Instruments Methods Phys. Res. Sect. B Beam Interact. with Mater. Atoms. 15 (1986) 760–764.

[33] A. Debelle, J.-P. Crocombette, A. Boulle, A. Chartier, T. Jourdan, S. Pellegrino, D. Bachiller-Perea, D. Carpentier, J. Channagiri, T.-H. Nguyen, F. Garrido, L. Thomé, Lattice strain in irradiated materials unveils a prevalent defect evolution mechanism, Phys. Rev. Mater. 2 (2018) 013604.

[34] A. Debelle, A. Declémy, L. Vincent, F. Garrido, L. Thomé, XRD contribution to the study of Cs-implanted cubic zirconia, J. Nucl. Mater. 396 (2010) 240–244.

[35] J. Channagiri, A. Boulle, A. Debelle, Determination of strain and damage profiles in irradiated materials: Application to cubic zirconia irradiated at high temperature, Nucl. Instruments Methods Phys. Res. Sect. B Beam Interact. with Mater. Atoms. 327 (2014) 9–14.

[36] G. Velişa, E. Wendler, H. Xue, Y. Zhang, W.J. Weber, Revealing ionization-induced dynamic recovery in ion-irradiated SrTiO3, Acta Mater. 149 (2018) 256–264.

[37] D.S. Zhou, O.. W. Holland, J.D. Budai, Strain relief mechanism for damage growth during high-dose , O+ implantation of Si, Appl. Phys. Lett. 63 (1993) 3580.

[38] F. Cristiano, A. Nejim, Y. Suprun-Belevich, A. Claverie, P.L.F. Hemment, Formation of extended defects and strain relaxation in ion beam synthesised SiGe alloys, Nucl. Instruments Methods Phys. Res. B. 147 (1999) 35–42.

[39] B. Vincent, J.-F. Damlencourt, V. Delaye, R. Gassilloud, L. Clavelier, Y. Morand, Stacking fault generation during relaxation of silicon germanium on insulator layers obtained by the Ge condensation technique, Appl. Phys. Lett. 90 (2007) 074101.

[40] M.A. Py, K. Maschke, Intra- and interlayer contributions to the lattice vibrations in MoO3, Phys. B+C. 105 (1981) 370–374.

[41] T.M. McEvoy, K.J. Stevenson, Spatially resolved imaging of inhomogeneous charge transfer behavior in polymorphous molybdenum oxide. I. Correlation of localized structural, electronic, and chemical properties using conductive probe atomic force microscopy and Raman microprobe spectros, Langmuir. 21 (2005) 3521–3528.

[42] L. Seguin, M. Figlarz, R. Cavagnat, J.-C. Lassègues, Infrared and Raman spectra of MoO3 molybdenum trioxides and MoO3. xH2O molybdenum trioxide hydrates, Spectrochim. Acta A. 51 (1995) 1323–1344.

[43] G. Mestl, N.F.D. Verbruggen, E. Bosch, H. Kno, Mechanically Activated MoO3. 5. Redox Behavior, Langmuir. 12 (1996) 2961–2968.

[44] G. Mestl, C. Linsmeier, R. Gottschall, M. Dieterle, J. Find, D. Herein, J. Jäger, Y. Uchida, R. Schlögl, Molybdenum oxide based partial oxidation catalyst: 1. Thermally induced oxygen deficiency, elemental and structural heterogeneity and the relation to catalytic performance, J. Mol. Catal. A Chem. 162 (2000) 463–492.

[45] K.A. Olson, G.L. Schrader, Laser deposition of molybdenum oxide thin films from organometallic precursors, Mater. Res. Soc. Symp. Proc. 187 (1990) 167–171.

[46] G. Mestl, In situ Raman spectroscopy for the characterization of MoVW mixed oxide catalysts, J. Raman Spectrosc. 33 (2002) 333–347.

[47] L. Kumari, Y.R. Ma, C.-C. Tsai, Y.-W. Lin, S.Y. Wu, K.-W. Cheng, Y. Liou, X-ray diffraction and Raman scattering studies on large-area array and nanobranched structure of 1D MoO2 nanorods, Nanotechnology. 18 (2007) 115717.

[48] R.K. Sharma, G.B. Reddy, Influence of O2 – plasma ambience and growth temperature on the oxidation of Mo-metal and volatilization of oxides, AIP Adv. 3 (2013) 092112.

[49] D. Wang, D.S. Su, R. Schlögl, Crystallographic Shear Defect in Molybdenum Oxides: Structure and TEM of Molybdenum Sub-oxides Mo18O52 and Mo8O23, Cryst. Res. Technol. 38 (2003) 153–159.

[50] D.E. Diaz-Droguett, A. Zuñiga, G. Solorzano, V.M. Fuenzalida, Electron beam-induced structural transformations of MoO3 and MoO3-x crystalline nanostructures, J. Nanoparticle Res. 14 (2012) 679.

[51] L.A. Bursill, Crystallographic Shear in Molybdenum Trioxide, Proc. R. Soc. A Math. Phys. Eng. Sci. 311 (1969) 267–290.

[52] J. Van Landuyt, Shear Structures and Crystallographic Shear Propagation, J. Phys. Colloq. 35 (1974) C7-53-C7-63.

[53] I. Navas, R. Vinodkumar, K.J. Lethy, A.P. Detty, V. Ganesan, V. Sathe, V.P.M. Pillai, Growth and characterization of molybdenum oxide nanorods by RF magnetron sputtering and subsequent annealing, J. Phys. D. Appl. Phys. 42 (2009) 175305.

[54] A. Blume, Synthesis and structural investigations from molybdenum, vanadium and to tungsten oxide for the heterogeneous catalysis, PhD thesis, Berlin Technical University, 2014.

[55] W.J. Weber, Models and mechanisms of irradiation-induced amorphization in ceramics, Nucl. Instruments Methods Phys. Res. B. 166–167 (2000) 98–106.

[56] S.J. Pearton, Ion implantation for isolation of III-V semiconductors, Mater. Sci. Reports. 4 (1990) 313–363.

[57] L. Vines, C. Bhoodoo, H. Von Wenckstern, M. Grundmann, Electrical conductivity of In2O3 and Ga2O3 after low temperature ion irradiation; Implications for instrinsic defect formation and charge neutrality level, J. Phys. Condens. Matter. 30 (2018) 025502.

[58] D. Xiang, C. Han, J. Zhang, W. Chen, Gap states assisted MoO3 nanobelt photodetector with wide spectrum response., Sci. Rep. 4 (2014).

[59] H.-S. Kim, J.B. Cook, H. Lin, J.S. Ko, S.H. Tolbert, V. Ozolins, B. Dunn, Oxygen vacancies enhance pseudocapacitive charge storage properties of MoO3-x, Nat. Mater. 16 (2017) 454–460.

[60] S. Balendhran, J. Deng, J.Z. Ou, S. Walia, J. Scott, J. Tang, K.L. Wang, M.R. Field, S. Russo, S. Zhuiykov, M.S. Strano, N. Medhekar, S. Sriram, M. Bhaskaran, K. Kalantar-Zadeh, Enhanced charge carrier mobility in two-dimensional high dielectric molybdenum oxide, Adv. Mater. 25 (2013) 109–114.

[61] Y. Bando, Y. Kato, T. Takada, Crystal Growth of Molybdenum Oxides by Chemical Transport, Bull. Inst. Chem. Res. Kyoto Univ. 54 (1976) 330–334.

[62] S. V Eremeev, M.G. Vergniory, T. V Menshchikova, A.A. Shaposhnikov, E. V Chulkov, The effect of van der Waal's gap expansions on the surface electronic structure of layered topological insulators, New J. Phys. 14 (2012) 113030.

[63] K. Inzani, M. Nematollahi, F. Vullum-Bruer, T. Grande, T.W. Reenaas, S.M. Selbach, Electronic properties of reduced molybdenum oxides, Phys. Chem. Chem. Phys. 19 (2017) 9232–9245.

[64] E. Wendler, E. Treiber, J. Baldauf, S. Wolf, C. Ronning, High-level damage saturation below amorphisation in ion implanted beta-Ga2O3, Nucl. Inst. Methods Phys. Res. B. 379 (2016) 85–90.

[65] N. Mejai, A. Debelle, L. Thomé, G. Sattonnay, D. Gosset, A. Boulle, R. Dargis, A. Clark, L. Thom, Depth-dependent phase change in Gd2O3 epitaxial layers under ion irradiation, Appl. Phys. Lett. 107 (2015) 131903.

[66] D.E. Diaz-Droguett, V.M. Fuenzalida, M.S. Diaz-Espinoza, G. Solorzano, Electron beam effects on amorphous molybdenum oxide nanostructures grown by condensation in hydrogen, J. Mater. Sci. 43 (2008) 591–596.